RSC Advances

PAPER

View Article Online
View Journal | View Issue

Cite this: *RSC Adv.*, 2023, **13**, 22863

Photothermal theranostics with glutathione depletion and enhanced reactive oxygen species generation for efficient antibacterial treatment†

Yuelan Wu,[ab] Xiaoxue Liu,[bc] Xiaoyu Zhang,[bc] Shuping Zhang,[cd] Panhong Niu *[d] and Hua Gao*[abc]

Received 16th May 2023
Accepted 24th July 2023

DOI: 10.1039/d3ra03246a

rsc.li/rsc-advances

Drug-resistant bacteria caused by the abuse of antibiotics have brought great challenges to antimicrobial therapy. Herein an antibiotic-free polydopamine (PDA) modified metal–organic framework (PDA-FDM-23) with photothermal-enhanced chemodynamic effect was developed for synergistic antibacterial treatment. The PDA-FDM-23 antibacterial agent exhibited high peroxidase-like activity. Moreover, the process was significantly accelerated by consuming glutathione (GSH) to generate more efficient oxidizing Cu^{+}. In addition, the photothermal therapy (PTT) derived from PDA improved the chemodynamic therapy (CDT) activity triggering a reactive oxygen species explosion. This PTT-enhanced CDT strategy illustrated 100% antibacterial efficiency against both *Staphylococcus aureus* and *Escherichia coli*. Cytotoxicity and hemolysis analyses fully demonstrated the excellent biocompatibility of PDA-FDM-23. Overall, our work highlighted the strong peroxidase catalytic activity, excellent GSH consumption and photothermal performance of PDA-FDM-23, providing a new strategy for antibiotic-free reactive oxygen species (ROS) synergistic sterilization.

1. Introduction

The misuse or high-dose use of antibiotics in clinical practice has led to the emergence and spread of drug-resistant bacteria, posing a great threat to population health.[1,2] Among them, *Staphylococcus aureus* (*S. aureus*) and *Escherichia coli* (*E. coli*) are the typical pathogens that cause various infections and even severe systemic diseases.[2,3] Thus, it is critical to develop novel and highly efficient antimicrobial strategies without using antibiotics.

Photothermal therapy (PTT) features the capability of damaging the integrity of pathogenic bacteria by generating hyperthermia to destroy the structure of a biofilm,[4] exhibiting the obvious advantage of non-invasive bacterial eradication without inducing resistance. However, the desirable curative treatment for anti-bacteria requires the high power of the excitation light and high dosage of photothermal agents,[5] which would damage normal tissues. Notably, the synergistic PTT and chemodynamic therapy (CDT) have received tremendous attention and exhibited cooperatively enhanced bactericidal activity,[6–9] especially only requiring low dosage of light irritation intensity, providing an available strategy for solving the above problems. CDT, which is based on the *in situ* conversion of hydrogen peroxide (H_2O_2) to highly toxic hydroxyl radicals ($^{\cdot}OH$) in lesions under the catalysis of Fenton agents, has been recognized as an emerging and efficient strategy for disease treatment,[10] such as tumor and antimicrobial therapy.[11–14] Particularly, the bactericidal action induced by ROS destroying bacterial membranes, DNA, protein and other components avoids the occurrence of drug resistance caused by antibiotic sterilization.[15–17] So far, despite Fe-based nanomaterials being the most used CDT agents, the amount of $^{\cdot}OH$ generated is insufficient to effectively kill pathogens.[7,18–20] Exploring novel and highly efficient CDT agents that can produce sufficient highly toxic ROS in response to the bacteria microenvironment is urgently needed for antibacterial applications.

Metal–organic frameworks (MOFs), possessing high specific surface area and porosity, and abundant active sites, exhibit attractive superiority in catalysis, gas storage and drug delivery.[21–23] Besides, the metal centers of MOFs can be released as metal ions during the degradation process of MOFs,[24] choosing a suitable metal ion that may be as effective CDT agents. As a mineral nutrient in the biological progresses,

[a]*Qingdao University, Qingdao, Shandong 266071, P. R. China. E-mail: hgao@sdfmu.edu.cn*

[b]*Eye Institute of Shandong First Medical University, State Key Laboratory Cultivation Base, Shandong Provincial Key Laboratory of Ophthalmology, Qingdao, Shandong 250071, P. R. China*

[c]*Medical Science and Technology Innovation Center, Shandong First Medical University & Shandong Academy of Medical Sciences, Jinan, Shandong 250117, P. R. China*

[d]*Biomedical Sciences College & Shandong Medicinal Biotechnology Centre, Shandong First Medical University & Shandong Academy of Medical Sciences, Jinan, 250117, P. R. China. E-mail: niupanhong@sdfmu.edu.cn*

† Electronic supplementary information (ESI) available. See DOI: https://doi.org/10.1039/d3ra03246a

copper ions possessed crucial biological functions such as cell signaling conduction, metalloallosteric regulating and energy metabolism.[25] More to mention that Cu^{+} is also found to have excellent Fenton-like catalytic activity and the reaction rate of Cu^{+} is much higher than that of Fe^{2+}, resulting in high ROS generation.[26,27] It is notable that the microenvironments of infection sites often have abnormally high glutathione (GSH) levels that are induced by anaerobic glycolysis.[27,28] Furthermore, the excess GSH in the infection sites could reduce the Cu(II) to Cu(I), then Cu(I) reacts with H_2O_2 to produce $^{\cdot}OH$, further accelerating the rate of Fenton reaction. Specially, Wang *et al.* reported that Cu-doped porous carbon acted as GSH peroxidase-like nanozymes significantly improving the sterilization effect by depleting GSH in bacteria.[27] However, the doping process is complicated, easy to fall off, and it is not easy to ensure the consistency of doping concentration. Therefore, choosing a MOF containing copper ions as the Cu-loading vehicle, in which the released copper ions can play a nanozyme role to consume GSH and enhance Fenton reaction, may be a promising strategy. Two-dimensional (2D) $Cu_6(C_8H_4O_4)_6(H_2O)_6\cdot H_3[P(W_3O_{10})_4]$ (FDM-23) MOF with ultrathin thickness and 2D morphology, was a Cu-based MOF exfoliated from 3D MOF, exhibiting notable electrocatalysis, sensing and separation performance.[29–32] It is expected that the released copper ions of 2D FDM-23 MOF can trigger GSH elimination, then catalyze Fenton-like reaction, significantly increasing the CDT effect.

Herein, we design a polydopamine (PDA) modified 2D FDM-23 MOF (PDA-FDM-23) for photothermal enhanced chemodynamic synergetic antibacterial therapy (Scheme 1). The introduction of PDA can employ near-infrared (NIR) light to induce mild photothermal effect to fight bacteria, and enhance the peroxidase-like catalytic activity, thereby generating additional $^{\cdot}OH$ to destroy bacteria.[27] As expected, PDA-FDM-23 has excellent GSH-depleting enhanced CDT performance, which can exert peroxidase catalytic activity while consuming GSH in bacteria to generate Cu^{+}, cascade-catalyze high-efficiency Fenton-like reactions, and significantly improve the antibacterial effect by generating abundant ROS. The antibacterial strategy of PTT synergistic GSH depletion-enhanced CDT produces almost 100% antibacterial efficiency against *S. aureus* and *E. coli*. Most importantly, this Cu-based MOF composite platform exhibits good biocompatibility, ensuring its potential for biomedical applications.

2. Materials and methods

2.1. Materials

Analytical grade copper(II) nitrate trihydrate ($Cu(NO_3)_2\cdot 3H_2O$), isophthalic acid (*m*-H_2BDC), phosphotungstic acid ($H_3[P(W_3O_{10})_4]$) and dopamine hydrochloride (DA-HCl) were purchased from Sigma-Aldrich Co., Ltd. (USA). Ammonia aqueous solution ($NH_3\cdot H_2O$, 28–30%) was obtained from Macklin Co., Ltd. (Shanghai, China). Aminomethane hydrochloride (Tris–HCl), methanol and *N*,*N*-dimethyl formamide were provided by Sinopharm Chemical Reagent Co., Ltd. (Shanghai, China). Cell Counting Kit-8 was purchased from MedChemExpress Co., Ltd. (Shanghai, China), and other biological reagents were purchased from Beyotime Biotechnology Co., Ltd. (Shanghai, China). Corneal epithelial cells (HCEC) and mouse fibroblasts (L-929) were provided by the Cell Bank of the Chinese Academy of Science (Shanghai, China).

2.2. Synthesis of PDA-FDM-23

The detailed synthesis steps were presented in Scheme 1. Firstly, 3D FDM-23 MOF nanocrystals were prepared according to the previously reported methods.[30,32] The preparation process of FDM-23 is as follows: 500 mg $Cu(NO_3)_2\cdot 3H_2O$, 350 mg *m*-H_2BDC, and 2.5 g $H_3[P(W_3O_{10})_4]$ were dissolved in 19 mL *N*,*N* dimethylformamide (DMF), 19 mL ethyl alcohol, and 13 mL

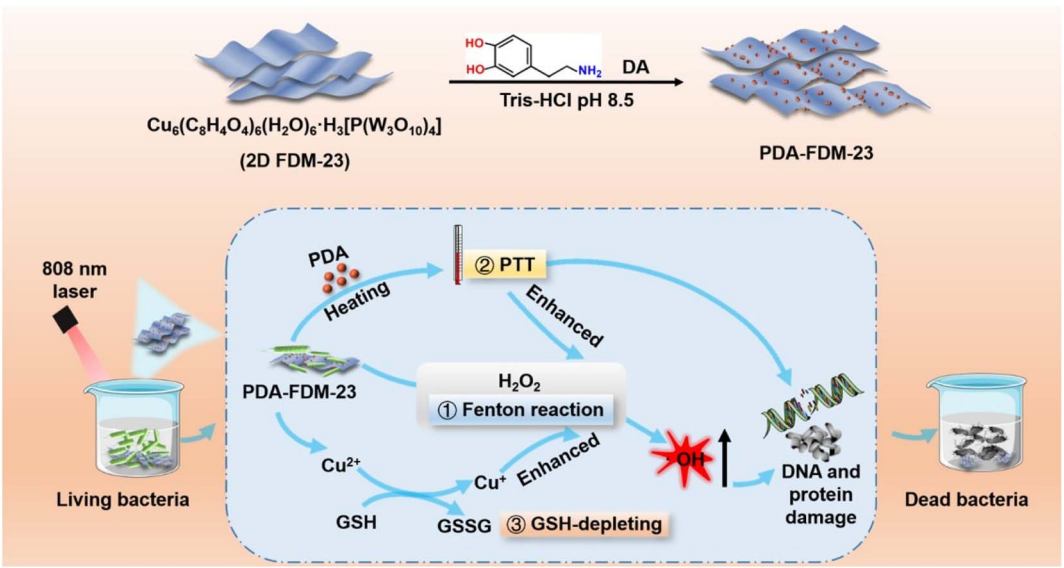

Scheme 1 Schematic illustration of the PDA-FDM-23 for photothermal-enhanced catalytic antibacterial therapy.

H_2O in a 100 mL vial for sonication treatment to ensure homogeneity. Then the above solution was heated at 85 °C in an oven for 24 h. The product was washed with H_2O several times and the blue crystals 3D FDM-23 MOF was obtained *via* filtration and drying in vacuum oven. Then the nanosheets of 2D FDM-23 were obtained by ultrasonic stripping. Briefly, 0.1 g of 3D FDM-23 MOF nanocrystals were added to 50 mL distilled water and sonicated continuously for 10 hours. After centrifugation, the supernatant was taken and lyophilized for 2 days to obtain 2D FDM-23. Subsequently, the PDA-FDM-23 composite was synthesized by using a solution oxidation method.[33] 0.01 g of 2D FDM-23 was taken to be dispersed in a Tris–HCl buffer solution (10 mM, pH 8.5, 20 mL), and then 0.02 g of DA-HCl was added to the above mixture and stirred continuously at room temperature for 24 hours. Finally, the PDA-FDM-23 nanosheets were collected by centrifugation (12 000 rpm, 15 min), washed with deionized water for three times, and then freeze-dried for further use.

2.3. Synthesis of PDA nanospheres

The PDA nanospheres with an average diameter of approximately 150 nm were synthesized by oxidation and self-polymerization of dopamine. 3 mL of aqueous ammonia solution ($NH_3 \cdot H_2O$, 28–30%), 40 mL of ethanol and 90 mL of deionized water were mixed and stirred at room temperature for 0.5 hours. 0.5 g of DA-HCl was dissolved in 10 mL of deionized water and then added to the above mixture solution. After 24 hours of reaction, the precipitate was taken out after centrifugation, and the obtained PDA nanospheres were washed three times with deionized water.

2.4. Characterizations of the nanodrugs

The morphological characterization of the as-prepared materials was performed by a transmission electron microscopy (HT7800, Hitachi, Japan). The hydrodynamic diameters and zeta potentials of particles were determined by a dynamic light scattering (DLS) particle size analyzer (Zetasizer Nano ZS90, Malvern, UK). The Fourier transform infrared spectroscopy (FT-IR) spectra were conducted by a Fourier transform infrared spectrometer (Nicolet iS5, Thermo Scientific, USA). The X-ray diffraction (XRD) patterns were collected using a Japan Rigaku Ultima IV diffractometer. And a UV-vis spectrophotometer (U3900H, Hitachi, Japan) was used to measure the UV-vis spectra of samples. X-ray photoelectron spectroscopy (XPS, Escalab 250Xi, ThermoScientific, USA) was employed to record the XPS spectra. The TGA curves were acquired with a thermal gravimetric analyzer (TG209 F3, Netzsch, Germany). The Cu content in the PDA-FDM-23 composite was determined by inductively coupled plasma-mass spectroscopy (ICP-MS, TQ, ThermoFisher, USA). The fluorescence images were collected by an inverted fluorescence microscope (Axio vert A1, Zeiss, Germany).

2.5. Photothermal effect of PDA, FDM-23 and PDA-FDM-23

To measure the photothermal conversion ability of the samples, the PDA-FDM-23 solutions containing different concentrations were irradiated with 808 nm near-infrared laser for 10 minutes. The PDA-FDM-23 solutions were then irradiated with near-infrared radiation of different power densities for 10 minutes. Photostability was determined by 5 laser on/off cycles of irradiation for 10 minutes and natural cooling to room temperature. The temperature changes during the experiment were collected and recorded by the infrared thermal imager (FLIR). The photothermal conversion efficiency of PDA-FDM-23 materials was calculated according to the following eqn (1)–(3) referring previous study.[34] The related parameters were shown in Table S1.†

$$\eta = \frac{hS(T_{max} - T_{suur})}{I\left(1 - 10^{-A_{808}}\right)} \quad (1)$$

$$hS = -\frac{\sum_i m_i C_i}{\tau_s} \quad (2)$$

$$\theta = \frac{T - T_{suur}}{T_{max} - T_{suur}} (\tau_s = 1.98) \quad (3)$$

where T_{max} is the maximum temperature of the PDA-FDM-23 solution, T_{suur} is the ambient temperature of the surrounding, A is the absorbance value of the PDA-FDM-23 solution at 808 nm ($A_{808} = 1.982$). hS was calculated using the following eqn (2); τ_s is the slope of the fitting line between cooling time t and $-\ln\theta$.

2.6. Peroxide-like catalytic activity of PDA-FDM-23

The formation of $^{\bullet}OH$ was investigated by methylene blue (MB) degradation experiment. In short, PDA-FDM-23 (100 μg mL^{-1}) was reacted with H_2O_2 (1 mM) in phosphate buffer solution at pH 7.4 under different conditions (with or without laser irradiation). The supernatant was collected after centrifugation. MB dye (10 μg mL^{-1}) was added and incubated for 0.5 h at 25 °C. The color change of the solution and the characteristic absorbance change at 660 nm were monitored. Then, the ability of PDA-FDM-23 to cascade-catalyze the generation of $^{\bullet}OH$ after completely exhausting GSH was explored. PDA-FDM-23 was incubated with 1 mM GSH for 2 hours to completely consume GSH, the precipitate was removed by centrifugation, H_2O_2 (1 mM) and MB (10 μg mL^{-1}) were added to react for 0.5 h, and the absorbance was detected. The POD-like catalytic activity of PDA-FDM-23 was investigated according to the method in the previous literature with some modifications.[35,36] The magnified initial linear portion of the nanozyme reaction-time curve of MB colorimetric reaction catalyzed by PDA-FDM-23. A length of 400 s was chosen for the initial rate period because the R^2 coefficients were close to 1 during this period after a linear-regression analysis. With catalyzed oxidation of PDA-FDM-23, the color of substrate MB gradually weakens and the absorbance value decrease. Thus, the absolute value of reaction rate was adopted to carry out the Michaelis–Menten curve. The Michaelis–Menten curves of PDA-FDM-23 was obtained as shown in Fig. S7,† which the MB concentration varied from 0 to 30 μg mL^{-1}. The kinetics constants ν_{max} and K_m were obtained by fitting the reaction velocity values and the substrate concentrations as following equation:

$$v = (v_{max} \times [S])/(K_m + [S])$$

where v is the initial reaction velocity and v_{max} is the maximal reaction rate that is observed at saturating substrate concentrations. [S] is the concentration of the substrate and K_m is the Michaelis constant.

2.7. GSH-depleting function of PDA-FDM-23

The consumption of GSH by PDA-FDM-23 was assessed using the 5,5′-dithiobis(2-nitrobenzoic acid) (DTNB) probe. Different concentrations of PDA-FDM-23 and GSH (1 mM) were mixed and sampled at different time points after the reaction. The supernatant was incubated with DTNB (0.1 mM) at 25 °C for 3 minutes, and the absorbance of the mixed solution was recorded with a multifunctional microplate reader.

2.8. Antibacterial performance evaluation

Gram-positive *S. aureus* and Gram-negative *E. coli* were cultured in fresh Luria-Bertani broth medium to logarithmic growth phase (37 °C, 200 rpm min^{-1}), and then the bacterial suspension was diluted to 10^6 colony forming units (CFU) per mL for further experiments. Different concentrations of PDA-FDM-23 or 100 μg mL^{-1} of different materials (PDA, FDM-23, PDA-FDM-23) were added to treat bacteria for 4 h respectively. Then, irradiation with near-infrared laser or without near-infrared laser (1.5 W cm^{-2}, 20 min) was performed, and PBS treatment group was used as a control. Then 100 μL treated bacterial suspension was taken from each group, diluted appropriately, smeared on solid medium to culture at 37 °C for 24 h. The bacterial CFU numbers were calculated by ImageJ software. All experiments were repeated three times independently.

2.9. Bacterial membrane integrity detection

The propidium iodide (PI) dye could smoothly pass through the cell membrane of dead bacteria. After different treatments, bacterial suspension (10^8 CFU mL^{-1}) was incubated for 4 h. Bacterial cells were then collected by centrifugation and stained with PI dye (30 μM) at room temperature for 20 min in the dark. The bacteria were washed 3 times with PBS and observed by fluorescence inverted fluorescence microscope.

2.10. Morphological observation of bacteria

The effects of different treatments on bacterial morphology were studied by scanning electron microscope (SEM). Bacterial samples from different groups were centrifuged and fixed in 1 mL of 2.5% glutaraldehyde for 4 hours and then stored at 4 °C overnight. The bacteria were dehydrated sequentially with increasing concentrations of ethanol (10, 30, 50, 70 and 90%) for 10 minutes. Subsequently, the dehydrated bacterial sample was dried at room temperature, sputter-coated with gold and characterized by SEM.

2.10.1. ROS detection in bacteria. The changes of ROS in bacteria were detected using 2′,7′-dichlorofluorescin diacetate (DCFH-DA) reactive oxygen species assay kit. Different treatment groups after laser irradiation/non-laser irradiation were stained with DCFH-DA (10 μM) for 30 minutes. The collect precipitate was washed 3 time with PBS and that green fluorescence was observed using fluorescence microscopy to detect ROS production.

2.11. Cytotoxicity assay

CCK-8 assay was employed to evaluate the cytotoxicity of different materials. HCEC and L-929 cells were incubated at 37 °C under 5% CO_2 in Dulbecco modified Eagle medium (DMEM)-F12 and DMEM with 10% fetal bovine serum and 1% penicillin–streptomycin, respectively. In short, 1×10^4 cells per well were seeded in 96-well microplates and cultured for 24 h. The cells were then cultured for 24 h after different drug treatments (with or without laser irradiation). Finally, the cells were treated with CCK-8 solution for 1–4 h and the optical density was measured at 450 nm using a multifunctional microplate reader.

2.12. Cell morphology observation

The cell morphology was viewed by fluorescence staining. Briefly, the cell slides were preinstalled in a 12-well plate, and cell suspension was added for culture for 24 hours. After the addition of different materials (PDA, FDM-23, PDA-FDM-23), the cells were exposed to laser light for 20 minutes (1.5 W cm^{-2}) or in the dark. After incubated at 37 °C for 1 day, washed with PBS for 3 times, and fixed with formaldehyde, the cell slides were stained with phalloidin FITC and DAPI, and observed under a laser confocal microscope.

2.13. Hemolytic analysis

Hemolysis experiment was carried out with fresh blood of 8 week-old female C57BL/6J mice. Red blood cells were collected at 10 000 rpm for 5 minutes and washed 5 times with PBS to completely remove white blood cells. 200 μL of red blood cells were aspirated and fixed to 10 mL with PBS to obtain a 2% red blood cell suspension. Next, red blood cell suspensions were added to equal volumes of PDA, FDM-23 or PDA-FDM-23 with different concentrations and incubated at room temperature for 4 h. After centrifugation at 10 000 rpm for 15 min, the absorbance (570 nm) of the supernatant was determined using a microplate reader. Deionized water group and PBS group were used as positive control group and negative control group respectively. The hemolysis rate was calculated as follows:

$$\text{Hemolysis } (\%) = \frac{A_{sample} - A_{negative}}{A_{positive} - A_{negative}} \times 100\%$$

2.14. Statistical analysis

All the data are expressed as the means ± SEM. Statistical significance was evaluated by Student's *t*-test for between two-group comparison and one-way ANOVA with Fisher's LSD for multiple-group analysis. *P*-value < 0.05 was considered statistically significant.

3. Results and discussion

3.1. Design and characterization of PDA-FDM-23

PDA-FDM-23 composite nanosheets were prepared according to the previously reported method.[30,32] The 2D MOF nanosheets were obtained by exfoliating the 3D MOF-FDM-23 crystals *via* ultrasonic treatment, and then the PDA was modified on the surface of the nanosheets by a simple self-assembly method. The TEM image of Fig. 1a revealed that the PDA was well-dispersed spherical particles with an average size of about 150 nm. After modified PDA, the lamellar microstructure of 2D FDM-23 remained unchanged, with an average diameter of about 500 nm (Fig. 1b). Moreover, the size of the PDA-FDM-23 nanosheet was determined by DLS which was significantly larger than the pure FDM-23 nanosheets due to the hydration (Fig. S1†), revealing the successfully modification of PDA on the nanosheet. The zeta potential of PDA-FDM-23 under physiological conditions (pH 7.4, PBS) had a higher absolute value (24.5 mV) than PDA and FDM-23, indicating the excellent stability of PDA-FDM-23 in solution (Fig. 1c).

FT-IR spectrums of PDA, 2D FDM-23 and PDA-FDM-23 were shown in Fig. 1d. The peaks at 3430 cm^{-1} were ascribed to the O–H stretching vibrations.[37,38] The peaks at 1610 cm^{-1} were assigned to the stretching vibrations of C=C in the benzene ring. In the FT-IR spectrum of PDA-FDM-23, the peaks at 1490 cm^{-1} and 1030 cm^{-1} were corresponded to the N–H shearing vibrations and C–O stretching, respectively, proving that PDA was successfully modified on the MOF surface. Notably, the representative COO– peak at 1390 cm^{-1} moved to 1260 cm^{-1} indicating the formation of a hydrogen bond between the amino group of PDA and carboxyl group of 2D FDM-23.[39] XRD characterization revealed that the patterns of FDM-23 and PDA-FDM-23 were basically consistent,[40] indicating that the crystallographic structure of FDM-23 was integrity without suffering destruction of post-modification (Fig. 1e). To further validate the successful synthesis of PDA-FDM-23, UV-vis absorption spectra of nanomaterials were investigated as shown in Fig. 1f. The FDM-23 shown strong absorption peak at about 250 nm below 400 nm, which indicated that the pure FDM-23 MOF displayed no visible light response.[41] The abnormal

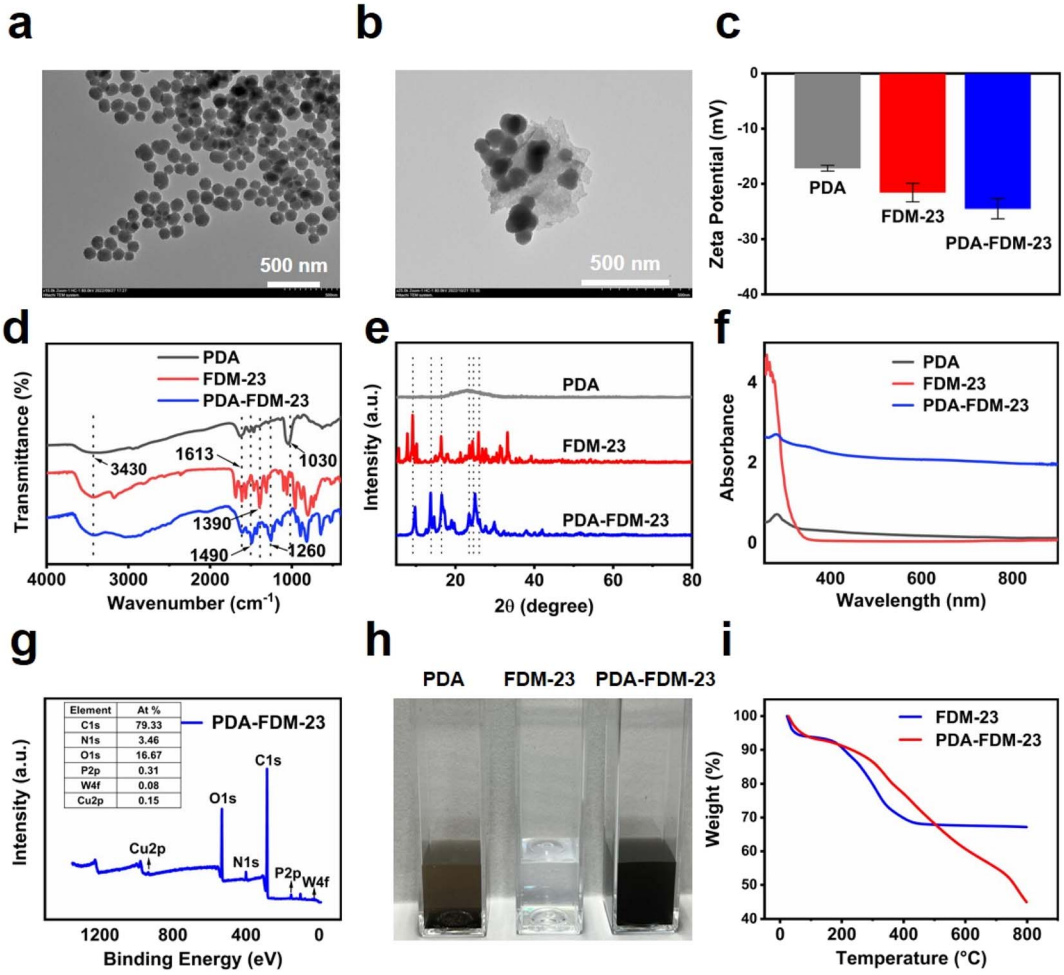

Fig. 1 Characterization of PDA-FDM-23. The representative TEM images of PDA (a) and PDA-FDM-23 (b). (c) The zeta potential of PDA, FDM-23 and PDA-FDM-23. (d) The FT-IR spectra of PDA, FDM-23, PDA-FDM-23. (e) The XRD results of PDA, FDM-23 and PDA-FDM-23. (f) The UV-vis absorption spectra of PDA, FDM-23 and PDA-FDM-23. (g) XPS survey spectra analysis of PDA-FDM-23. (h) Representative images of PDA, FDM-23 and PDA-FDM-23 dispersed in water. (i) Thermogravimetric analysis of FDM-23 and PDA-FDM-23.

values of FDM-23 absorption curve below 300 nm was due to the strong UV absorption of FDM-23 MOF structure. On the contrary, the pure PDA exhibited strong absorption performance at about 280 nm.[42] After decorating PDA onto FDM-23 MOF, the UV-vis diffuse reflectance spectra of PDA-FDM-23 composites shows the absorption characteristics of two components. Meanwhile, the enhanced absorbance of PDA-FDM-23 in the near infrared region compared with FDM-23 was the premise of photothermal therapy, resulting in higher photothermal efficiency.[43] SEM-EDS elemental mapping analysis disclosed that the two synthesized MOF materials were composed of C, N, O, P, W and Cu, which were uniformly distributed throughout the nanosheets (Fig. S2†). And as illustrated in the XPS analysis (Fig. 1g and S3a†), the chemical bond peaks located at 36 eV, 134 eV, 284 eV, 401 eV, 531 eV and 934 eV originated from W 4f, P 2p, C 1s, N 1s, O 1s, and Cu 2p,[38] respectively. The atomic percentage provided in the XPS spectrum confirmed the presence of Cu element. The spectrum of Cu 2p could be deconvolved into two individual peaks (Fig. S3b and c†), located at near 934 eV and 932 eV respectively, corresponding to Cu^{2+} ($2p_{3/2}$) and Cu^{+} ($2p_{3/2}$).[44] The existence of Cu^{+} might be ascribed to the partial reduction reaction during the synthesis of FDM-23. To be expected, PDA-FDM-23 containing copper ions as the Cu-loading vehicle can released copper ions to consume GSH and enhance Fenton reaction, collaborating PTT to achieve enhanced antibacterial therapy.

3.2. Dispersion and stability of PDA-FDM-23

The dispersion stability of PDA, FDM-23 and PDA-FDM-23 composites in deionized water was monitored by sedimentation experiment (Fig. 1h). The original PDA showed significant subsidence after 30 min ultrasound dispersion. In contrast, PDA-FDM-23 solution had less agglomeration and could maintain good dispersion. This can be interpreted that the large aperture and specific surface area of the layered FDM-23 facilitated the dispersion of the PDA nanoparticles. Then, the FDM-23 and PDA-FDM-23 were subjected to thermogravimetric analysis to obtain stability information (Fig. 1i). When the temperature was increased to 200 °C, the weight of PDA-FDM-23 began to drop, which was assigned to the decomposition of PDA,[45] suggesting the outstanding stability of PDA-FDM-23 under physiological conditions.

3.3. Photothermal effect of PDA-FDM-23

According to the analysis result of the UV-vis absorption spectrum, the composite PDA-FDM-23 still maintained a good absorption in the NIR region, which endowed it with great potential for photothermal therapy. Therefore, we systematically explored its photothermal conversion properties. As shown in Fig. 2a, the temperature of PDA-FDM-23 solution raised with the increase of concentration under the irradiation of NIR laser (808 nm, 1.5 W cm^{-2}). Particularly, the temperature of the 100 μg mL^{-1} group could reach 50.1 °C after 10 min of irradiation, which was in accordance with the reported photothermal temperature.[46] Furthermore, the PDA-FDM-23 composite material showed obvious dependence on laser power, and a significant temperature rise was observed at an intensity of 1.5 W cm^{-2} (Fig. S4†). The photothermal stability of antibacterial agent was also an important index for evaluating the photothermal property for practical application. It could be found that the PDA-FDM-23 solution could be stably heated to about 50 °C after five consecutive heating and cooling cycles (Fig. 2b), and the absorbance value has no significant decrease before and after irradiation (Fig. S5†), which further proved the high photostability of PDA-FDM-23. In addition, photothermal curves (Fig. 2c) and infrared images (Fig. 2d) demonstrated that the PDA-modified FDM-23 retained the ability to convert light energy into thermal energy. More to mention that, the photothermal efficiency of PDA-FDM-23 was higher than PDA at an equivalent dose, which was due to the improved dispersibility facilitating the thermogenesis.[39] The photothermal conversion efficiency of PDA-FDM-23 was calculated to be as high as 17.26% (as shown in Fig. S6†). The PDA-FDM-23 photothermal agent, possessing improved dispersibility, high photostability and enhanced photothermal conversion ability, would be beneficial to enhance photothermal antibacterial therapy.

3.4. Peroxidase-like activity and GSH-depleting function

Previous studies suggested that Cu-MOF had peroxidase-like activity, which can catalyze H_2O_2 to produce ROS,[47–49] rendering them promising CDT agents for antibacterial therapy. To investigate the CDT capability of as-prepared PDA-FDM-23, MB was adopted as an indicator of $^{\bullet}OH$ that produced from CDT catalytic reaction. Blue MB exhibited a fading phenomenon after oxidation by $^{\bullet}OH$ resulting the decrease of absorbance value at 660 nm. As shown in Fig. 2e, compared with the inconspicuous changes in absorbance value induced by PDA-FDM-23, PDA-FDM-23 + H_2O_2 showed a significant decrease, indicating that PDA-FDM-23 had strong peroxidase-like catalytic activity to catalyze H_2O_2 to produce ROS. The Michaelis constant K_m value was obtained by fitting the reaction velocity as shown in Fig. S7,† which was 11.24 μM. Moreover, the PDA-FDM-23 displayed more significant catalytic activity under NIR laser irradiation, suggesting that ionization at elevated temperatures accelerated the efficiency of the Fenton-like reaction.[50]

The peroxidase-like catalytic activity of PDA-FDM-23 correlated with H_2O_2 in a dose-dependent manner (Fig. 2f). With the increase of H_2O_2 concentration, the degradation of MB was more obvious owing to the gradual production of $^{\bullet}OH$. Interestingly, PDA-FDM-23 still maintained its catalytic activity for H_2O_2 (Fig. 2e) after GSH exhaustion, with a stronger trend. We speculate that this effect may result from that the Cu^{2+} in PDA-FDM-23 consumes glutathione through redox reaction. As a Fenton-like reagent, Cu^{+} generated in this process show high-efficient catalytic ability, further improving the level of $^{\bullet}OH$.[15,51–53] The free copper ions of PDA-FDM-23 can deplete the environmental GSH of infections and amplify the oxidative stress of $^{\bullet}OH$, resulting in enhanced antibacterial effects. Thus, we employed ICP-MS to confirm the release of copper ions from PDA-FDM-23 over time. Fig. 2g revealed the sustained release of copper ions in PBS solution and enhancement after laser

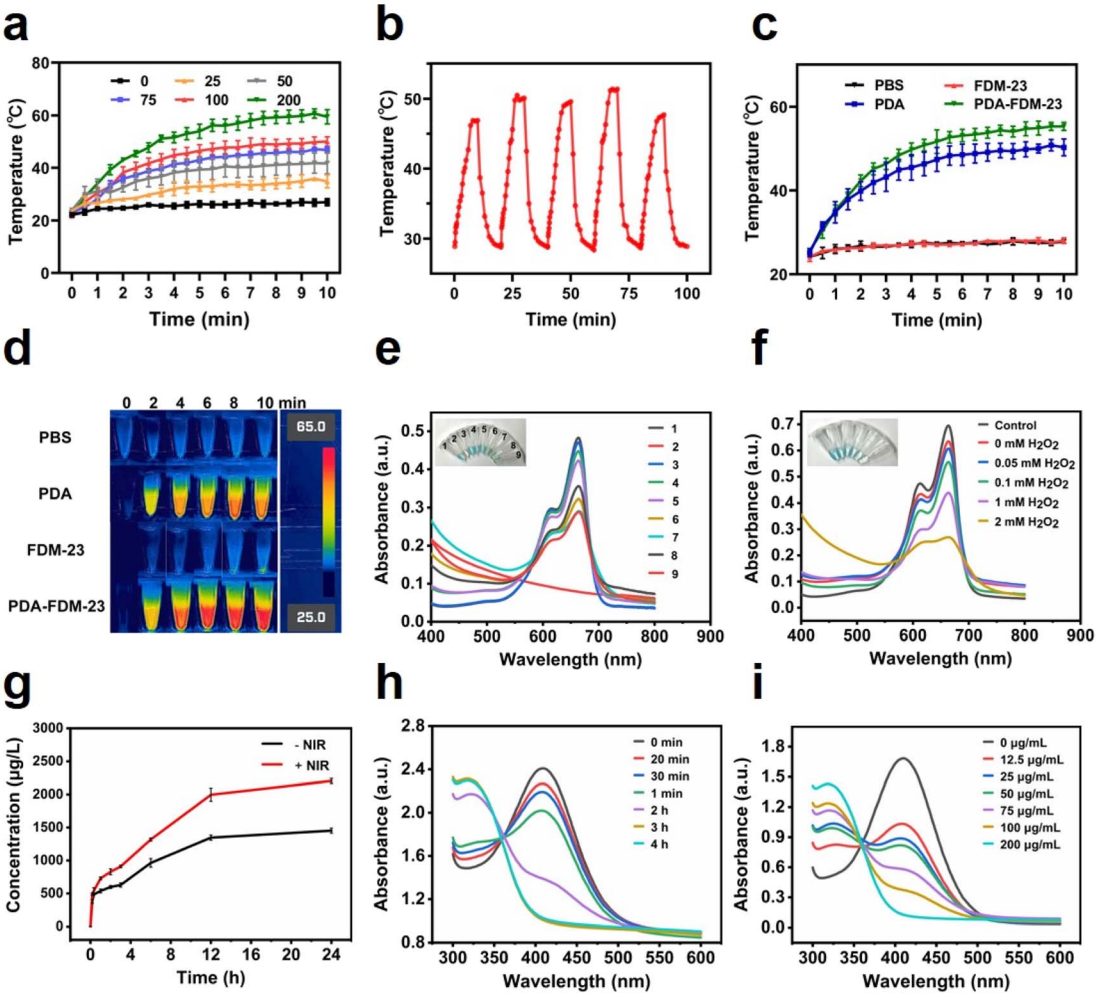

Fig. 2 Photothermal properties, peroxidase-like activity and GSH-depleting function of PDA-FDM-23. (a) Temperature elevation of different concentrations of PDA-FDM-23 (0, 25, 50, 75, 100 and 200 μg mL^{-1}) measured under an 808 nm NIR laser (1.5 W cm^{-2}). (b) Temperature change of 100 μg mL^{-1} PDA-FDM-23 during five cycles of on/off NIR laser irradiation. (c) Photothermal curves of different materials (PDA, FDM-23 and PDA-FDM-23) at a concentration of 100 μg mL^{-1}. (d) Infrared thermography of PDA, FDM-23 and PDA-FDM-23. (e) Evaluation of ˙OH generation ability of PDA-FDM-23 under different treatments with MB probe ((1) MB; (2) PDA-FDM-23 + H_2O_2; (3) H_2O_2 + MB; (4) PDA-FDM-23 + MB; (5) PDA-FDM-23 + NIR + MB; (6) PDA-FDM-23 + H_2O_2 + MB; (7) PDA-FDM-23 + H_2O_2 + NIR + MB; (8) PDA-FDM-23 + GSH + H_2O_2 + MB; (9) PDA-FDM-23 + GSH + H_2O_2 + NIR + MB). (f) MB degradation ability of PDA-FDM-23 in the presence of different concentrations of H_2O_2. (g) The release of copper ions over time as measured by ICP-MS under laser (+NIR) and non-laser illumination (−NIR). The GSH depletion ability of PDA-FDM-23 determined by DTNB probe at different times (h) and different concentrations (i).

irradiation, laying the foundation for the potential function of PDA-FDM-23. Then, we monitored the GSH-depleting ability of PDA-FDM-23 using a DTNB probe, which was reduced by GSH with characteristic change in absorbance at 412 nm. After adding GSH, the absorption peak of DTNB at 412 nm gradually weakened and almost disappeared after 3 h (Fig. 2h), indicating that PDA-FDM-23 possessed GSH-depleting properties in a concentration-dependent manner (Fig. 2i).

Taken together, the remarkable photothermal performance, peroxidase-like catalytic performance of PDA-FDM-23 and GSH depletion function complemented and reinforced each other to generate abundant ROS, showing a great application prospect in synergistic antibacterial therapy.

3.5. Synergistic antibacterial performance of PDA-FDM-23

Considering the excellent properties mentioned above, the synergistic antibacterial properties of PDA-FDM-23 *in vitro* were comprehensively evaluated using Gram-positive bacterial *S. aureus* and Gram-negative bacterial *E. coli* as representative models. Firstly, the photothermal antibacterial effect of PDA-FDM-23 under non-laser and laser irradiation (1.5 W cm^{-2}, 20 min) was separately investigated by plate counting method (Fig. S8a and b†). Obviously, under dark conditions, PDA-FDM-23 could inhibit both bacteria to some extent, and the antibacterial effect relied on the concentration of PDA-FDM-23, which might be derived from the peroxidase-like activity of PDA-FDM-23 itself. After the introduction of laser, the survival rates of *S. aureus* and *E. coli* treated with 100 μg mL^{-1} PDA-FDM-

23 were only 15.6% and 0.45%, respectively, and no bacteria survived at 200 μg mL^{-1}, which confirmed the important role of laser irradiation in the catalytic antibacterial activity of PDA-FDM-23. Then, to further highlight the synergistic antibacterial function of PDA-FDM-23, the antibacterial capabilities of different materials in the absence and presence of laser irradiation were compared with each other. As presented in Fig. 3a and b, compared to the blank control, the viable count of PDA was slightly reduced regardless of laser irradiation, indicating that the photothermal conversion performance of PDA could not support the killing of bacteria by PDA alone. Besides, the similarity of the number of unmodified FDM-23 colonies to that of PDA suggested that FDM-23 could not exert the antibacterial effect due to its slight antibacterial function and almost no photothermal conversion ability. Surprisingly, although the bactericidal effect of PDA-FDM-23 without laser treatment was weak, the antibacterial rates of PDA-FDM-23 exposed to laser against both *S. aureus* and *E. coli* reached 100%, revealing that the broad-spectrum photothermal antibacterial effect of PDA-FDM-23 was superior to that of FDM-23 and PDA alone.

To elucidate the mechanism of PDA-FDM-23 against bacteria, the integrity of the bacterial membrane was assessed using PI. The cell membrane of the dead bacteria could not prevent PI dye from entering the nucleus due to the loss of selective permeability. According to the results of Fig. 3c and S9,† the laser-treated PDA-FDM-23 group had the highest number of bacterial deaths compared to the other treated groups, demonstrating that the PDA-FDM-23 we prepared had remarkable cell membrane destruction capability, which was also in line with the plate counting results. And SEM observation of bacterial morphology showed that the bacteria in the other treatment groups had a complete and smooth outer

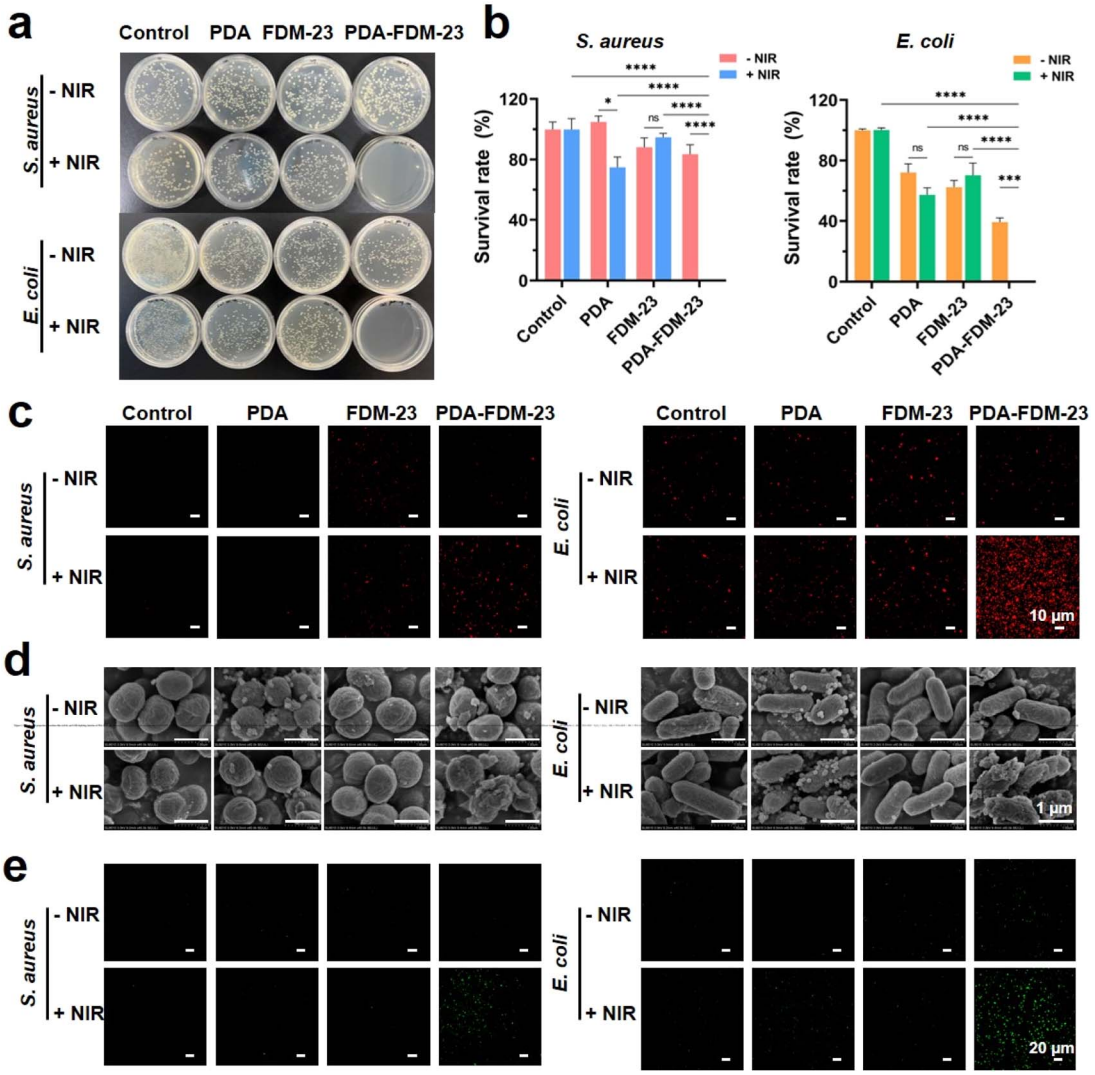

Fig. 3 Evaluation of antibacterial activity of PDA-FDM-23. (a) The plate count images of different materials (PDA, FDM-23 and PDA-FDM-23) after treatment with or without light (concentration: 100 μg mL^{-1}, laser power: 1.5 W cm^{-2}, 20 min). (b) Relative bacterial survival rates of *S. aureus* and *E. coli* after various treatments. (c) Fluorescence-stained images of *S. aureus* and *E. coli* with PI after different treatments. (d) SEM images of *S. aureus* and *E. coli* in different treatment groups. (e) Typical fluorescence images of ROS stained by DCFH-DA in *S. aureus* and *E. coli* under different treatments. Data were represented as means ± SEM ($n = 3$). ns: no significant difference, ****$P < 0.0001$, ***$P < 0.001$, *$P < 0.1$.

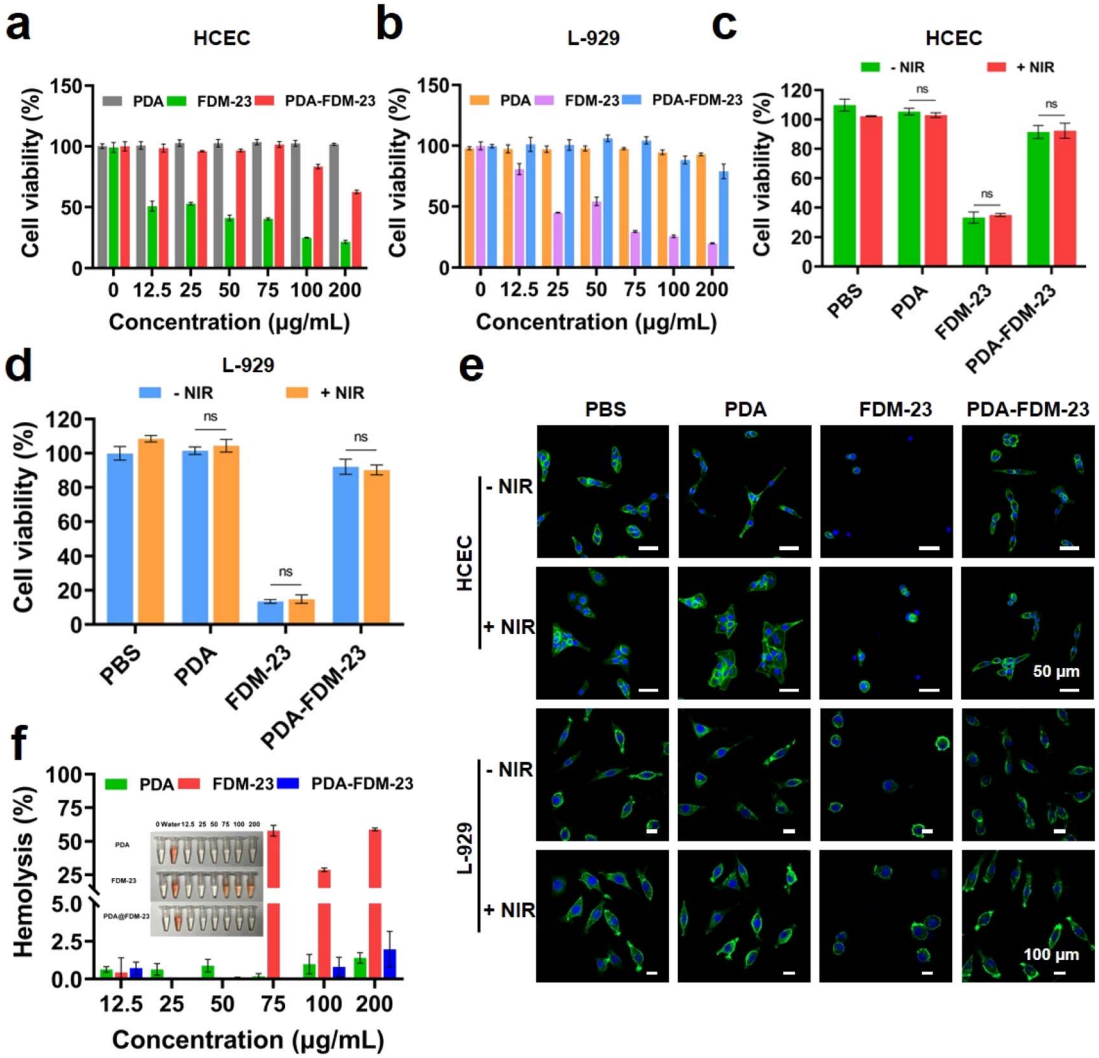

Fig. 4 Biocompatibility analysis of PDA-FDM-23. (a and b) Cytotoxicity of HCEC and L-929 cells with PDA-FDM-23 treated for 24 h. (c and d) Relative activities of HCEC cells and L-929 cells treated with various materials (100 μg mL^{-1}) without or with NIR laser irradiation (λ = 808 nm, 1.5 W cm^{-2}). (e) Fluorescent staining images of different materials incubated with HCEC and L-929 cells for 24 h. Green was the FITC-phalloidin labeled cytoskeleton and blue was the DAPI-stained nucleus. (f) Hemolysis analysis and representative image of PDA, FDM-23 and PDA-FDM-23 in various concentrations on erythrocyte suspension. Data were represented as means ± SEM (n = 3). ns: no significant difference.

membrane, similar to the natural living bacteria. However, after laser treatment of PDA-FDM-23, the bacteria wrinkled and the framework completely collapsed, further illustrating the bacterial membrane rupture effect mediated by photothermal and reactive oxygen species (Fig. 3d). More importantly, the level of ROS closely associated with bacterial death was carried out by DCFH-DA probe. As expected, the PDA-FDM-23 near-infrared synergistic treatment group exhibited the strongest ROS fluorescence, indicating that PDA-FDM-23 combined with near-infrared treatment could effectively produce ROS in bacteria (Fig. 3e and S10†).

Based on the above results, the following possible PDA-FDM-23 synergistic antibacterial mechanisms are summarized: (1) PDA-FDM-23 exerts peroxidase-like activity to catalyze endogenous H_2O_2 to produce toxicity $^{\cdot}OH$ to damage bacterial cell wall; (2) mild photo-thermal action directly destroys bacteria and accelerates the catalytic effect of PDA-FDM-23 through ionization; (3) the depletion of GSH by PDA-FDM-23 weakens the scavenging of ROS by micro-environment in bacteria, and the resulting Cu^+ increases the generation of ROS through more efficient Fenton reaction. Therefore, PDA-FDM-23 can be regarded as a promising synergistic antibacterial therapeutic agent.

3.6. Biocompatibility of PDA-FDM-23

Biocompatibility of antibacterial materials was essential for utilization in biomedical applications.[54,55] The cytotoxicity was investigated using Cell Counting Kit-8 assay with HCEC and L-929. As displayed in Fig. 4a and b, the high concentration of PDA with strong cell activity demonstrated the good biocompatibility of PDA, while the apparent toxicity of FDM-23 at low concentrations might be attributable to cell damage caused by

metal ions.[56] Hopefully, the PDA-modified FDM-23 group exhibited notably improved cell activity relative to FDM-23, with the activity still exceeding 80% at 100 μg mL^{-1}. Meanwhile, in order to eliminate the effect of laser on cells, we measured the cytotoxicity of different materials with or without laser irradiation. No significant differences were found with or without laser irradiation, suggesting the excellent biosafety of photothermal antibacterial agent PDA-FDM-23 (Fig. 4c and d). And the results of cell morphology staining further validated the cell compatibility of PDA-FDM-23. Except for cell shrinkage in the PDA-FDM-23-incubated group, the cell morphology of the other groups was unchanged in contrast with normal cells, regardless of laser illumination (Fig. 4e). Additionally, blood compatibility was another index to judge the safety of biomaterials besides cytotoxicity. According to the results in Fig. 4f, unlike the FDM-23 material leading to severe hemolysis, PDA-FDM-23 maintained conspicuous blood compatibility even at high concentrations. All the above results certified the feasibility of PDA-FDM-23 composite as a safe and excellent antibacterial nanoplatform for photothermal catalytic antibacterial treatment.

4. Conclusions

In this study, we successfully developed a multifunctional GSH-depleting photothermal catalytic nanomaterial consisting of PDA nanosheets and 2D FDM-23 nanosheets self-assembly. The obtained PDA-FDM-23 not only exhibits excellent peroxidase-like activity to decompose H_2O_2 to generate $^{\cdot}OH$, but also shows remarkable photothermal performance to directly damage bacterial membranes, and simultaneously improve the catalytic efficiency of the peroxidase-like enzyme. In addition, it can also effectively enhance the generation of $^{\cdot}OH$ through strong glutathione consumption, and has a satisfactory killing effect on both Gram-positive bacteria and Gram-negative bacteria. More importantly, the good biocompatibility of the synthesized PDA-FDM-23 endows it with the feasibility of safe biological applications. In conclusion, our work provides a promising strategy for clinical photothermal enhanced chemodynamic synergetic antibacterial therapy.

Conflicts of interest

The authors declare that they have no known competing financial interests or personal relationships that could have appeared to influence the work reported in this paper.

Acknowledgements

This work was financially supported by the Natural Science Foundation of Shandong (ZR2021QB171), the National Natural Science Foundation of China (82070923, 22076104 and 81870639), the Taishan Scholars Program (201812150 and 202103105) and the "Outstanding University Driven by Talents" Program and Academic Promotion Program of Shandong First Medical University (2020LJ002 and 2019RC009). We thank Ms Tong Liu for her linguistic and editorial assistance.

References

1 X. Wang, D. Peng, W. Wang, Y. Xu, X. Zhou and T. Hesketh, Massive misuse of antibiotics by university students in all regions of China: implications for national policy, *Int. J. Antimicrob. Agents*, 2017, **50**, 441–446.
2 E. Prina, O. T. Ranzani and A. Torres, Community-acquired pneumonia, *Lancet*, 2015, **386**, 1097–1108.
3 M. Xu, Y. Xiao, Y. Zhang, K. Sun, T. Wu, N. Lv, W. Wang, W. Ding, F. Li, B. Qiu and J. Li, Near-infrared-controlled nanoplatform exploiting photothermal promotion of peroxidase-like and OXD-like activities for potent antibacterial and anti-biofilm therapies, *ACS Appl. Mater. Interfaces*, 2020, **12**, 50260–50274.
4 J. W. Xu, K. Yao and Z. K. Xu, Nanomaterials with a photothermal effect for antibacterial activities: an overview, *Nanoscale*, 2019, **11**, 8680–8691.
5 J. Huo, Q. Jia, H. Huang, J. Zhang, P. Li, X. Dong and W. Huang, Emerging photothermal-derived multimodal synergistic therapy in combating bacterial infections, *Chem. Soc. Rev.*, 2021, **50**, 8762–8789.
6 Z. Liu, X. Zhao, B. Yu, N. Zhao, C. Zhang and F. J. Xu, Rough Carbon-Iron Oxide Nanohybrids for Near-Infrared-II Light-Responsive Synergistic Antibacterial Therapy, *ACS Nano*, 2021, **15**, 7482–7490.
7 F. Li, K. Huang, H. Chang, Y. Liang, J. Zhao, S. Yang and F. Liu, A polydopamine coated nanoscale FeS theranostic platform for the elimination of drug-resistant bacteria *via* photothermal-enhanced Fenton reaction, *Acta Biomater.*, 2022, **150**, 380–390.
8 Y. Qi, S. Ren, J. Ye, Y. Tian, G. Wang, S. Zhang, L. Du, Y. Li, Y. Che and G. Ning, Infection microenvironment-activated core-shell nanoassemblies for photothermal/chemodynamic synergistic wound therapy and multimodal imaging, *Acta Biomater.*, 2022, **143**, 445–458.
9 X. Zhang, Q. Qu, W. Cheng, A. Zhou, Y. Deng, W. Ma, M. Zhu, R. Xiong and C. Huang, A Prussian blue alginate microparticles platform based on gas-shearing strategy for antitumor and antibacterial therapy, *Int. J. Biol. Macromol.*, 2022, **209**, 794–800.
10 L. H. Fu, Y. Wan, C. Qi, J. He, C. Li, C. Yang, H. Xu, J. Lin and P. Huang, Nanocatalytic theranostics with glutathione depletion and enhanced reactive oxygen species generation for efficient cancer therapy, *Adv. Mater.*, 2021, **33**, e2006892.
11 Z. Tang, Y. Liu, M. He and W. Bu, Chemodynamic Therapy: Tumour Microenvironment-Mediated Fenton and Fenton-like Reactions, *Angew. Chem., Int. Ed. Engl.*, 2019, **58**, 946–956.
12 B. Niu, K. Liao, Y. Zhou, T. Wen, G. Quan, X. Pan and C. Wu, Application of glutathione depletion in cancer therapy: Enhanced ROS-based therapy, ferroptosis, and chemotherapy, *Biomaterials*, 2021, **277**, 121110.
13 C. Jia, Y. Guo and F. G. Wu, Chemodynamic Therapy *via* Fenton and Fenton-Like Nanomaterials: Strategies and Recent Advances, *Small*, 2022, **18**, e2103868.

14 L. Zhang, C. X. Li, S. S. Wan and X. Z. Zhang, Nanocatalyst-Mediated Chemodynamic Tumor Therapy, *Adv. Healthcare Mater.*, 2022, **11**, e2101971.

15 H. Shi, C. Ban, C. Dai, C. Li, X. Zhou, R. Xia, J. Qian and M. Cao, Glutathione-depletion reinforced enzyme catalytic activity for photothermal assisted bacterial killing by hollow mesoporous CuO, *J. Mater. Chem. B*, 2022, **10**, 8883–8893.

16 J. Xi, G. Wei, L. An, Z. Xu, Z. Xu, L. Fan and L. Gao, Copper/Carbon Hybrid Nanozyme: Tuning Catalytic Activity by the Copper State for Antibacterial Therapy, *Nano Lett.*, 2019, **19**, 7645–7654.

17 H. Liu, J. Li, X. Liu, Z. Li, Y. Zhang, Y. Liang, Y. Zheng, S. Zhu, Z. Cui and S. Wu, Photo-Sono Interfacial Engineering Exciting the Intrinsic Property of Herbal Nanomedicine for Rapid Broad-Spectrum Bacteria Killing, *ACS Nano*, 2021, **15**, 18505–18519.

18 L. Zhang, S. S. Wan, C. X. Li, L. Xu, H. Cheng and X. Z. Zhang, An Adenosine Triphosphate-Responsive Autocatalytic Fenton Nanoparticle for Tumor Ablation with Self-Supplied H_2O_2 and Acceleration of Fe(III)/Fe(II) Conversion, *Nano Lett.*, 2018, **18**, 7609–7618.

19 Z. Tang, P. Zhao, H. Wang, Y. Liu and W. Bu, Biomedicine Meets Fenton Chemistry, *Chem. Rev.*, 2021, **121**, 1981–2019.

20 X. Yu, T. Shang, G. Zheng, H. Yang, Y. Li, Y. Cai, G. Xie and B. Yang, Metal-polyphenol-coordinated nanomedicines for Fe(II) catalyzed photoacoustic-imaging guided mild hyperthermia-assisted ferroustherapy against breast cancer, *Chin. Chem. Lett.*, 2022, **33**, 1895–1900.

21 L. Ma, F. Jiang, X. Fan, L. Wang, C. He, M. Zhou, S. Li, H. Luo, C. Cheng and L. Qiu, Metal-Organic-Framework-Engineered Enzyme-Mimetic Catalysts, *Adv. Mater.*, 2020, **32**, e2003065.

22 T. Ghanbari, F. Abnisa and W. M. A. Wan Daud, A review on production of metal organic frameworks (MOF) for CO_2 adsorption, *Sci. Total Environ.*, 2020, **707**, 135090.

23 H. D. Lawson, S. P. Walton and C. Chan, Metal-Organic Frameworks for Drug Delivery: A Design Perspective, *ACS Appl. Mater. Interfaces*, 2021, **13**, 7004–7020.

24 P. Zhang, Y. Li, Y. Tang, H. Shen, J. Li, Z. Yi, Q. Ke and H. Xu, Copper-based metal-organic framework as a controllable nitric oxide-releasing vehicle for enhanced diabetic wound healing, *ACS Appl. Mater. Interfaces*, 2020, **12**, 18319–18331.

25 A. P. Kornblatt, V. G. Nicoletti and A. Travaglia, The neglected role of copper ions in wound healing, *J. Inorg. Biochem.*, 2016, **161**, 1–8.

26 B. Ma, S. Wang, F. Liu, S. Zhang, J. Duan, Z. Li, Y. Kong, Y. Sang, H. Liu, W. Bu and L. Li, Self-Assembled Copper-Amino Acid Nanoparticles for *In Situ* Glutathione "AND" H_2O_2 Sequentially Triggered Chemodynamic Therapy, *J. Am. Chem. Soc.*, 2019, **141**, 849–857.

27 X. Wang, Q. Shi, Z. Zha, D. Zhu, L. Zheng, L. Shi, X. Wei, L. Lian, K. Wu and L. Cheng, Copper single-atom catalysts with photothermal performance and enhanced nanozyme activity for bacteria-infected wound therapy, *Bioact. Mater.*, 2021, **6**, 4389–4401.

28 M. Xu, Y. Hu, Y. Xiao, Y. Zhang, K. Sun, T. Wu, N. Lv, W. Wang, W. Ding, F. Li, B. Qiu and J. Li, Near-Infrared-Controlled Nanoplatform Exploiting Photothermal Promotion of Peroxidase-like and OXD-like Activities for Potent Antibacterial and Anti-biofilm Therapies, *ACS Appl. Mater. Interfaces*, 2020, **12**, 50260–50274.

29 B. Wang, H. Li, H. Tan, Y. Gu, L. Chen, L. Ji, Z. Sun, Q. Sun, S. Ding, D. W. Zhang and H. Zhu, Gate-Modulated High-Response Field-Effect Transistor-Type Gas Sensor Based on the MoS_2/Metal-Organic Framework Heterostructure, *ACS Appl. Mater. Interfaces*, 2022, **14**, 42356–42364.

30 T. Si, X. Liang, X. Lu, L. Wang, S. Wang and Y. Guo, 2D metal-organic framework nanosheets-assembled core-shell composite material as stationary phase for hydrophilic interaction liquid chromatography, *Talanta*, 2021, **222**, 121603.

31 F. Mu, B. Dai, W. Zhao, L. Zhang, J. Xu and X. Guo, A review on metal-organic frameworks for photoelectrocatalytic applications, *Chin. Chem. Lett.*, 2020, **31**, 1773–1781.

32 A. Hu, Q. Pang, C. Tang, J. Bao, H. Liu, K. Ba, S. Xie, J. Chen, J. Chen, Y. Yue, Y. Tang, Q. Li and Z. Sun, Epitaxial growth and integration of insulating metal-organic frameworks in electrochemistry, *J. Am. Chem. Soc.*, 2019, **141**, 11322–11327.

33 R. Zheng, S. Wang, Y. Tian, X. Jiang, D. Fu, S. Shen and W. Yang, Polydopamine-Coated Magnetic Composite Particles with an Enhanced Photothermal Effect, *ACS Appl. Mater. Interfaces*, 2015, **7**, 15876–15884.

34 F. Li, K. Huang, H. Chang, Y. Liang, J. Zhao, S. Yang and F. Liu, A polydopamine coated nanoscale FeS theranostic platform for the elimination of drug-resistant bacteria *via* photothermal-enhanced Fenton reaction, *Acta Biomater.*, 2022, **150**, 380–390.

35 B. Jiang, D. Duan, L. Gao, M. Zhou, K. Fan, Y. Tang, J. Xi, Y. Bi, Z. Tong, G. F. Gao, N. Xie, A. Tang, G. Nie, M. Liang and X. Yan, Standardized assays for determining the catalytic activity and kinetics of peroxidase-like nanozymes, *Nat. Protoc.*, 2018, **13**, 1506–1520.

36 H. Dong, W. Du, J. Dong, R. Che, F. Kong, W. Cheng, M. Ma, N. Gu and Y. Zhang, Depletable peroxidase-like activity of Fe_3O_4 nanozymes accompanied with separate migration of electrons and iron ions, *Nat. Commun.*, 2022, **13**, 5365.

37 B. Gao, L. Chen, Y. Zhao, X. Yan, X. Wang, C. Zhou, Y. Shi and W. Xue, Methods to prepare dopamine/polydopamine modified alginate hydrogels and their special improved properties for drug delivery, *Eur. Polym. J.*, 2019, **110**, 192–201.

38 M. Maruthapandi, A. Saravanan, P. Das, M. Natan, G. Jacobi, E. Banin, J. H. T. Luong and A. Gedanken, Antimicrobial Activities of Zn-Doped CuO Microparticles Decorated on Polydopamine against Sensitive and Antibiotic-Resistant Bacteria, *ACS Appl. Polym. Mater.*, 2020, **2**, 5878–5888.

39 D. Han, Y. Li, X. Liu, K. W. K. Yeung, Y. Zheng, Z. Cui, Y. Liang, Z. Li, S. Zhu, X. Wang and S. Wu, Photothermy-strengthened photocatalytic activity of polydopamine-modified metal-organic frameworks for rapid therapy of bacteria-infected wounds, *J. Mater. Sci. Technol.*, 2021, **62**, 83–95.

40 X. Cheng, S. Zhang, H. Liu, H. Chen, J. Zhou, Z. Chen, X. Zhou, Z. Xie, Q. Kuang and L. Zheng, Biomimetic Metal-Organic Framework Composite-Mediated Cascade Catalysis for Synergistic Bacteria Killing, *ACS Appl. Mater. Interfaces*, 2020, **12**, 36996–37005.

41 H. Hu, K. Zhang, G. Yan, L. Shi, B. Jia, H. Huang, Y. Zhang, X. Sun and T. Ma, Precisely decorating CdS on Zr-MOFs through pore functionalization strategy: A highly efficient photocatalyst for H_2 production, *Chin. J. Catal.*, 2022, **43**, 2332–2341.

42 J. F. Huang, J. Zhong, G. P. Chen, Z. T. Lin, Y. Deng, Y. L. Liu, P. Y. Cao, B. Wang, Y. Wei, T. Wu, J. Yuan and G. B. Jiang, A hydrogel-based hybrid theranostic contact lens for fungal Keratitis, *ACS Nano*, 2016, **10**, 6464–6473.

43 L. S. Lin, Z. X. Cong, J. B. Cao, K. M. Ke, Q. L. Peng, J. H. Gao, H. H. Yang, G. Liu and X. Y. Chen, Multifunctional Fe_3O_4@Polydopamine Core-Shell Nanocomposites for Intracellular mRNA Detection and Imaging-Guided Photothermal Therapy, *ACS Nano*, 2014, **8**, 3876–3883.

44 S. Mo, Y. Zhao, J. Wen, J. Sun, Z. Zhang, Q. Yu, G. Wang, X. Chen and M. Liu, Efficient photothermal and photodynamic synergistic antibacterial therapy of Cu(7)S(4) nanosheets regulated by facet engineering, *J. Hazard. Mater.*, 2022, **432**, 128662.

45 Z. Shen, X. Zhou, H. Qiu, H. Xu, H. Chen and H. Zhou, A Comparison Study of Antiultraviolet and Sustained Release Properties of Polydopamine/Avermectin Microcapsule and Microsphere, *Int. J. Polym. Sci.*, 2018, **2018**, 1–13.

46 D. Hu, L. Zou, B. Li, M. Hu, W. Ye and J. Ji, Photothermal Killing of Methicillin-Resistant Staphylococcus aureus by Bacteria-Targeted Polydopamine Nanoparticles with Nano-Localized Hyperpyrexia, *ACS Biomater. Sci. Eng.*, 2019, **5**, 5169–5179.

47 S. Wang, W. Deng, L. Yang, Y. Tan, Q. Xie and S. Yao, Copper-Based Metal-Organic Framework Nanoparticles with Peroxidase-Like Activity for Sensitive Colorimetric Detection of Staphylococcus aureus, *ACS Appl. Mater. Interfaces*, 2017, **9**, 24440–24445.

48 R. Zhou, X. Zhuang, Q. Wu, M. Jin, C. Zheng, Y. Jiang, Y. Lou and L. Zheng, Cu-MOF@Pt 3D nanocomposites prepared by one-step wrapping method with peroxidase-like activity for colorimetric detection of glucose, *Colloids Surf., B*, 2022, **216**, 112601.

49 Y. Liu, W. Zhen, L. Jin, S. Zhang, G. Sun, T. Zhang, X. Xu, S. Song, Y. Wang, J. Liu and H. Zhang, All-in-One Theranostic Nanoagent with Enhanced Reactive Oxygen Species Generation and Modulating Tumor Microenvironment Ability for Effective Tumor Eradication, *ACS Nano*, 2018, **12**, 4886–4893.

50 X. Zhao, X. He, A. Hou, C. Cheng, X. Wang, Y. Yue, Z. Wu, H. Wu, B. Liu, H. Li, J. Shen, C. Tan, Z. Zhou and L. Ma, Growth of Cu(2)O Nanoparticles on Two-Dimensional Zr-Ferrocene-Metal-Organic Framework Nanosheets for Photothermally Enhanced Chemodynamic Antibacterial Therapy, *Inorg. Chem.*, 2022, **61**, 9328–9338.

51 E. Ju, K. Dong, Z. Chen, Z. Liu, C. Liu, Y. Huang, Z. Wang, F. Pu, J. Ren and X. Qu, Copper(II)-Graphitic Carbon Nitride Triggered Synergy: Improved ROS Generation and Reduced Glutathione Levels for Enhanced Photodynamic Therapy, *Angew. Chem., Int. Ed. Engl.*, 2016, **55**, 11467–11471.

52 C. Liu, D. Wang, S. Zhang, Y. Cheng, F. Yang, Y. Xing, T. Xu, H. Dong and X. Zhang, Biodegradable Biomimic Copper/Manganese Silicate Nanospheres for Chemodynamic/Photodynamic Synergistic Therapy with Simultaneous Glutathione Depletion and Hypoxia Relief, *ACS Nano*, 2019, **13**, 4267–4277.

53 R. Cao, W. Sun, Z. Zhang, X. Li, J. Du, J. Fan and X. Peng, Protein nanoparticles containing Cu(II) and DOX for efficient chemodynamic therapy *via* self-generation of H_2O_2, *Chin. Chem. Lett.*, 2020, **31**, 3127–3130.

54 M. Liu, H. Zhu, Y. Wang, C. Sevencan and B. L. Li, Functionalized MoS_2-Based Nanomaterials for Cancer Phototherapy and Other Biomedical Applications, *ACS Mater Lett*, 2021, **3**, 462–496.

55 D. Peng, G. Liu, Y. He, P. Gao, S. Gou, J. Wu, J. Yu, P. Liu and K. Cai, Fabrication of a pH-responsive core-shell nanosystem with a low-temperature photothermal therapy effect for treating bacterial biofilm infection, *Biomater. Sci.*, 2021, **9**, 7483–7491.

56 B. Ouyang, F. Liu, C. Liang, J. Zhang, R. Hu, H. Yuan, R. Hai, Y. Yuan, X. Wu and S. T. Yang, Toxicity and activity inhibition of metal-organic framework MOF-199 to nitrogen-fixing bacterium Azotobacter vinelandii, *Sci. Total Environ.*, 2022, **813**, 151912.